Flow, Turbulence and Combustion **72:** 391–406, 2004.

Vortex Dipoles Impinging on Finite Aspect Ratio Rectangular Obstacles*

IONUT DANAILA
Laboratoire Jacques-Louis Lions, Université Pierre et Marie Curie, Paris, France;
E-mail: danaila@ann.jussieu.fr

Received 20 June 2003; accepted in revised form 14 December 2003

Abstract. Numerical simulations of a vortex dipole rebound from finite aspect ratio rectangular obstacles are presented. Compared to the dipole interaction with infinite flat walls studied by Orlandi (*Phys. Fluids* **A2** (1990) 1429) new phenomena are observed. Secondary dipoles formed after the first rebound can undergo head-on collisions and partner exchange. A new lifting dipole is generated, moving in the opposite direction of the initial dipole. This phenomenon occurs for a ratio between the half-width of the obstacle and the dipole radius lower than a critical value depending on the Reynolds number of the flow. Scatter plots show a quasi-linear vorticity-stream function relationship for the lifting dipole. Some passive control strategies to inhibit the generation of lifting dipoles are also suggested.

Key words: vortex, dipole, Lamb-Chaplygin, boundary body-force

1. Introduction

Two-dimensional pairs of vortices of opposite signs (also called *couples*) are flow configurations encountered in many areas of practical interest (meteorological and coastal flows, trailing vortices from aircraft, 2D turbulence, swirled injection in stratified charge engines). One of the most popular flow model for a vortex couple is the Lamb–Chaplygin dipole [1, 2], analytically derived as an exact solution of the incompressible 2D Euler equations. Close approximations of this flow were obtained in laboratory experiments [3–5] and subsequently compared to accurate numerical simulations [6–9]. In particular, the topic of vortex dipoles impinging on boundaries has received a great deal of attention in the past two decades. Joint experimental and numerical investigations concerned the interaction of Lamb–Chaplygin dipoles with solid flat walls [6, 10] or circular cylinders [7, 8].

The purpose of the present contribution is to complete the picture of the dipole-wall interaction by considering another fundamental class of obstacles, the finite aspect-ratio rectangular shapes. Besides the potentially practical interest in this subject, this study is motivated by more fundamental questions concerning the dynamics of vortex dipoles impinging on flat walls of comparable size.

*Video animations of the simulations presented in this paper and more dipole-obstacle interaction simulations can be found on author's web page http://www.ann.jussieu.fr/∼danaila.

2. Numerical Model

We use the NTMIX3D code [11] solving the compressible Navier–Stokes equations with a highly accurate explicit finite difference scheme over a Cartesian grid. A third order low storage Runge–Kutta method [12] is used for time advancement and a spectral-like sixth-order compact scheme [13] for space derivatives computation. Non-reflecting boundary conditions are prescribed using the characteristics method proposed by [14].

The obstacles are immersed in the computational domain and mimicked using the *boundary-body force (BF) method*. The BF method try to bring the fluid at rest on the surface of the modelled body by applying a boundary-like treatment *inside* the computational domain and not at its borders as usually done. This is achieved by explicitly prescribing the force acting on the fluid flow due to the presence of the solid body. Suitable volume forces are numerically introduced as source terms in the Navier–Stokes equations. These forces are such calculated as to yield a controlled value $\vec{V}_{\text{body}}$ of the velocity on the surface of the mimicked solid body ($\vec{V}_{\text{body}} \neq 0$ for moving bodies). The volume force field $\vec{f}$ acts only inside the body ($\vec{f} \equiv 0$ for the external fluid flow) and can be prescribed in several ways [15–18].

For this study we use the method proposed by Mohd-Yusof [19] which has the advantage to preserve the stability characteristics of the basic Cartesian solver. This approach has recently achieved a remarkable success for incompressible flow calculations [20, 21]. Although this method is very simple and effective, to our knowledge, it was never applied to compressible flows. We therefore briefly present an extension of the method to the compressible NTMIX solver.

The compressible Navier–Stokes equations, written in their general form include a volumic source term $\vec{f}$ in the momentum equations, which is generally derived from a potential (e.g. gravity). The idea of the body-force method is to impose such an external force field to mimic the presence of solid bodies.

The force field will be thus function of time and space and will act only on the cells corresponding to the modelled body. The procedure introduced by Mohd–Yosof [19] uses a discrete *time-derivation* of the forcing to fix the velocity at a desired value. We apply this technique only for the momentum conservation equations. For a generic Runge–Kutta time advancement scheme, one can write the discretized momentum equations as:

$$\mathbf{Y}(t_{\text{n}} + \alpha\Delta t) = \mathbf{Y}(t_{\text{n}}) + \beta\Delta t[\mathbf{RHS}(t_{\text{n}}) + \vec{f}(t_{\text{n}})], \quad \mathbf{Y} = \rho\vec{V} \tag{1}$$

where RHS contains the nonlinear terms, pressure and viscous terms. If the value $\mathbf{Y}_b = \rho\vec{V}_{\text{body}}$ must be imposed at the time instant $t_{\text{n}} + \alpha\Delta t$, the body force vector will be calculated as:

$$\vec{f}(t_{\text{n}}) = \frac{\mathbf{Y}_b(t_{\text{n}} + \alpha\Delta t) - \mathbf{Y}(t_{\text{n}})}{\beta\Delta t} - \mathbf{RHS}(t_{\text{n}}) \tag{2}$$

It should be noted that in the compressible formulation, the contribution of this external force must be taken into account in the energy conservation equation.

This contribution, added as a source term $\vec{f} \cdot \vec{V}_{\text{body}}$, represents the work of the external force field and is non-zero only for moving bodies. As it stands, the body-force method will create adiabatic walls: it only pushes the surrounding flow. One can imagine a similar procedure to maintain the temperature at a desired value (isothermal walls) by using local heating in the energy conservation equation. In the following calculations, only adiabatic walls were generated by this technique.

The fully explicit formulation used by the NTMIX solver makes the implementation of the body-force method straightforward. Nevertheless, some particular issues must be discussed in the following.

The body-force vector must be carefully evaluated inside the low-storage Runge–Kutta procedure. We recall that the body-force $\vec{f}$ is calculated only for grid-points inside the modelled bodies and only for the momentum equations. For the computations presented in this paper, obstacle contours follow grid lines and no interpolation procedure is needed to evaluate the body-force. When moving walls are present, interpolation methods are necessary and the contribution to the energy equation must be calculated in order to have a correct formulation of the method.

Another important point that must be discussed here is the behavior of the body-force method when high order schemes are used for the spatial discretization. The sixth order compact scheme used by the NTMIX code has spectral accuracy and no artificial dissipation. Introducing point forces (singularities) in a spectral-like representation will trigger unrealistic spatial oscillations (see also [16]). We found, however, that these oscillations did not grow in an unstable manner in time and did not affect the realistic trend of the flow development. The most natural way to remove these short-wavelength oscillations was to apply a compact low-pass filter. The sixth-order compact filter [13] was chosen for its lower value of the cut-off wave-number.

The above described implementation of the body-force method do not affect the main computational features of the original NTMIX code (vectorization). The additional CPU time required to compute the body-force vector is negligible compared to the effective total CPU time of a simulation.

3. Flow Configuration

The Lamb-Chaplygin dipole [1, 2, 9] corresponds to a steady solution of the two-dimensional Euler equations. The structure of the dipole consists of two zones of opposite signed vorticities, symmetrically arranged about the line of motion. The dipole propagates with a constant (in the inviscid limit) translation velocity by a self-induction mechanism.

A typical flow configuration considered in this study is displayed on Figure 1. The vorticity ω of the dipole is concentrated in a circle of radius a and vanishes outside:

$$\omega_{\text{in}} = k^2 \psi_{\text{in}}, \quad r \leq a, \quad \omega_{\text{out}} = 0, \quad r > a. \tag{3}$$

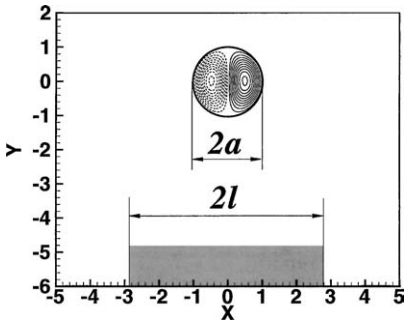

Figure 1. Flow configuration at $t = 0$. The Lamb–Chaplygin dipole of radius a is represented by contours of vorticity (dashed for negative).

For a dipole moving along the negative y-axis, the corresponding stream-function ($\omega = -\Delta\psi$) writes in cylindrical coordinates (r, θ):

$$\psi_{\text{in}} = C J_1(kr)\cos\theta, \qquad r \leq a \tag{4}$$

where J_1 is the first order Bessel function and C a parameter giving the intensity of the dipole. The exterior flow is an irrotational uniform flow, with constant velocity at infinity equal to the translation velocity of the dipole (V_c):

$$\psi_{\text{out}} = -V_c\left(r - \frac{a^2}{r}\right)\cos\theta, \qquad r > a \tag{5}$$

Note that ($u = 0$, $v = V_c$) for $r \to \infty$. Matching the two solutions at the circular boundary $r = a$ requires:

$$\psi_{\text{in}}|_{r=a} = \psi_{\text{out}}|_{r=a} \longrightarrow J_1(ka) = 0. \tag{6}$$

The first zero of the Bessel function J_1 corresponds to $ka \approx 3.83$. The translation velocity is obtained by imposing the continuity of the tangential velocity $u_\theta = -\partial\psi/\partial r$:

$$V_c = -\frac{C}{2}kJ_1'(ka) \approx -0.771\frac{C}{a} \tag{7}$$

Note that the radial velocity is also continuous at $r = a$:

$$v_r = \frac{1}{r}\frac{\partial\psi}{\partial\theta} = 0.$$

For the following simulations, the characteristic scales for length and velocity are set equal to 1. The radius of the dipole is fixed to $a = 1$ and the characteristic velocity of the dipole to $U^* = C/a = 0.1$, leading to a translation velocity $V_c = -0.0771$. The Reynolds number of the flow will be defined as in [6]: $Re = U^*a/\nu$.

The computational domain (Figure 1) is defined for $-5 \leq x \leq 5$ and $-6 \leq y \leq 2$. At $t = 0$, the dipole is centered at $x = y = 0$ and has self-induced downward translation velocity. The rectangular obstacle is symmetric with respect to the y-axis

and has a fixed height of 1. The ratio l/a between the half-width l of the obstacle and the dipole radius is the main parameter of this study.

As boundary conditions we used non-slip adiabatic wall conditions for the lower ($y = -6$) boundary and non-reflecting characteristics based conditions elsewhere. We remind that the obstacle is modelled by the BF method, imposing $\vec{V}_{\text{body}} = 0$ at all grid-points inside the obstacle. A refined grid using 320×400 nodes is employed, which is sufficient to achieve grid-independence for all considered numerical experiments.

4. Dipole Impinging on Infinite Flat Walls

As a first test of the numerical method, we consider the case of an obstacle extending through the whole width of the computational domain ($l/a = 5$). This test is two-fold:

1. We first check that a *classical* simulation (without the BF method) with a non-slip wall at $y = -5$ gives the same results; the two simulations are identical (pictures not shown) showing that the compact-filter used to remove the small amplitude wiggles introduced by the BF method does not affect the physical behavior of the flow (see also [16]).
2. As $l \gg a$, the results using the BF method are compared to those published by Orlandi [6] for a dipole impinging on infinite flat walls. The results are in excellent agreement (Figure 2) and will be discussed in the following.

The early evolution of the simulated flow is the uniform translation of the dipole towards the obstacle. It is interesting to note that the choice of the non-reflecting boundary conditions allows a physically realistic translation of the vortex dipole. The translation velocity measured for $t < 4$ is constant and approaches the theoretical value (V_c) within 1%. This was not the case in the simulations of [9] where the dipole was slowed down by the effect of periodic boundary conditions.

The dipole rebound (see Figure 2) is typically characterized by the viscous generation of secondary vorticity at the wall ($t = 7$). Primary vortices of the initial dipole ($\mathcal{D}0$) detach the (opposite sign) wall-generated vorticity ($t = 9$), leading to the formation ($t = 11$) of two new vortex couples ($\mathcal{D}1$ and $\mathcal{D}2$) moving away from the wall on circular paths ($t = 13$).

As the trajectory of a vortex couple is bent toward the stronger one, the subsequent interactions are controlled by the Reynolds number of the flow. Low Reynolds numbers evolution ($Re = 800$) displays new dipoles ($\mathcal{D}1$ and $\mathcal{D}2$) dominated by very strong primary vortices. Their trajectories are consequently very 'tighten' ($t = 15$) and, as the distance between the couples is large, their mutual interaction is weak: the secondary vortices form a new couple ($\mathcal{D}3$) which is trapped near the wall ($t = 17 - 19$).

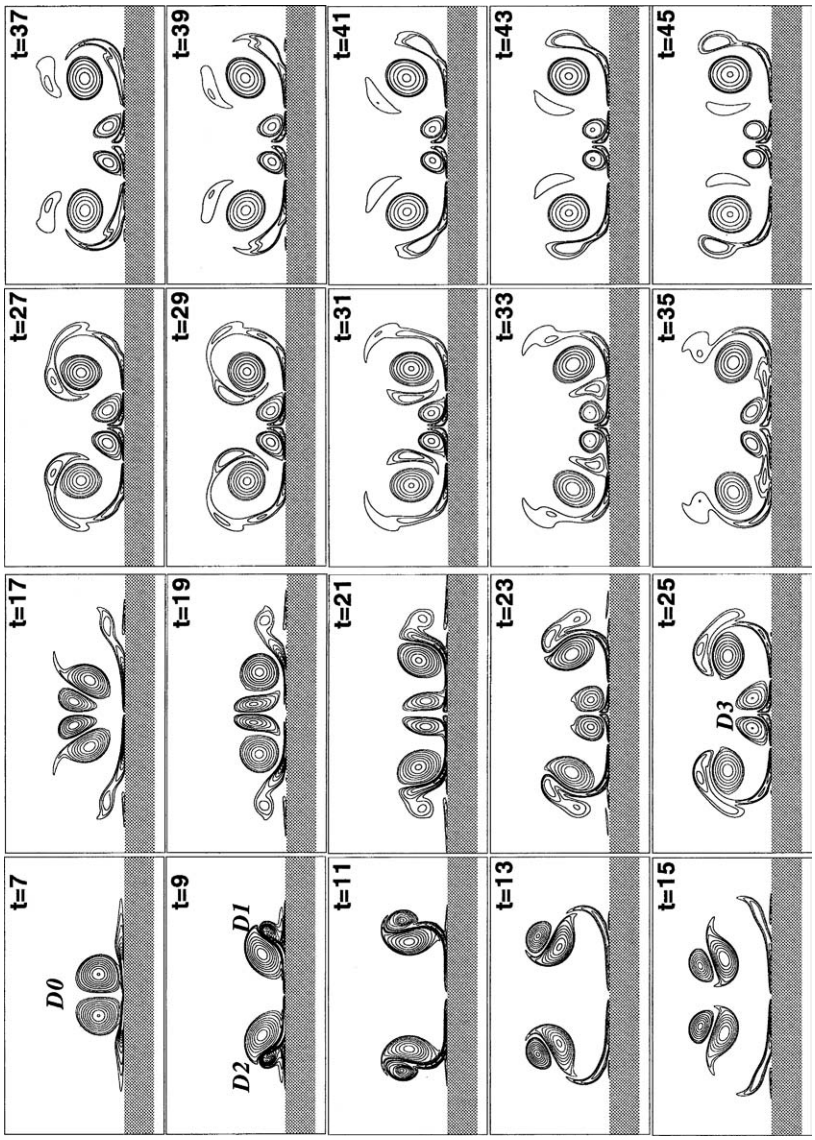

Figure 2. $Re = 800, l/a = 5$. Vorticity contours (dashed for negative).

The next stages ($t > 21$) of the flow evolution show several detachments of the wall-vorticity leading to new couples of vortices that are still dominated by primary vortices, moving far from the wall on circular trajectories. The successive layers of secondary vorticity entrained by primary vortices will merge with the $\mathcal{D}3$ dipole, which is finally dissipated by viscosity.

For higher Reynolds number ($Re = 1600$), Orlandi [6] reported an interesting phenomenon at this point of the flow evolution. Lower dissipation of the secondary

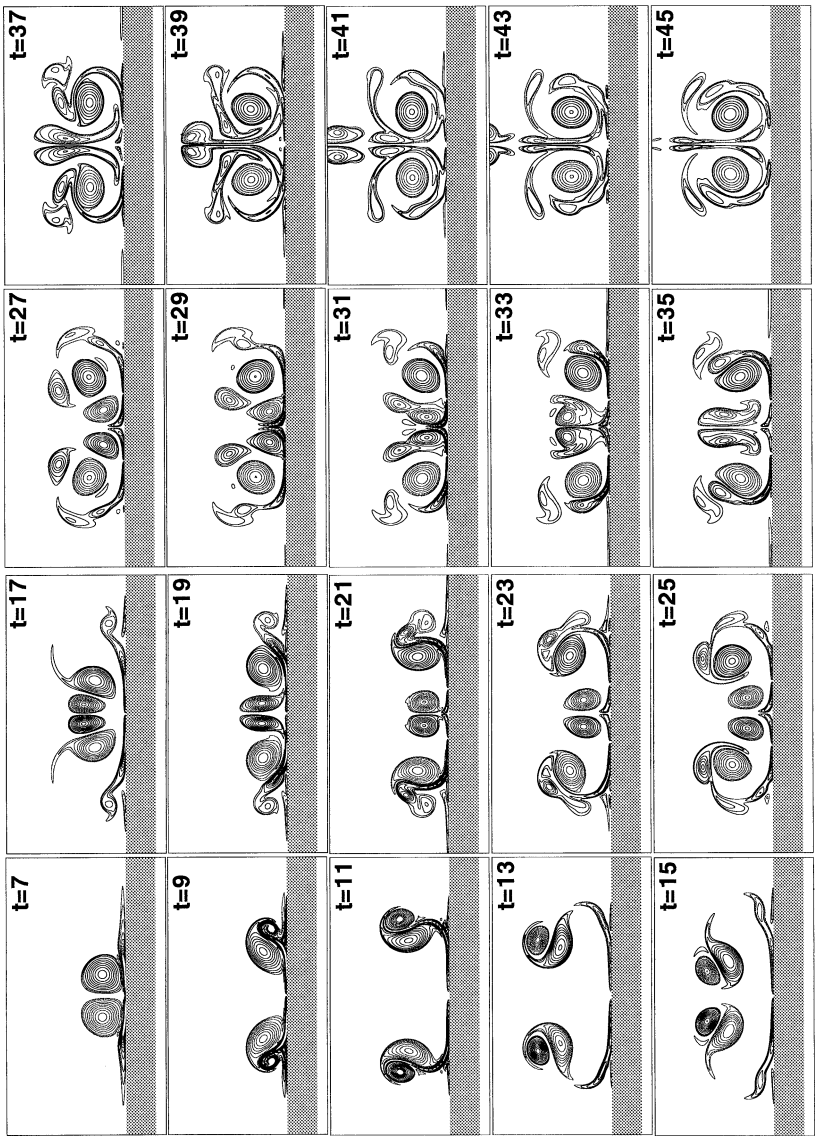

Figure 3. $Re = 1600, l/a = 5$. Vorticity contours.

vortices leads to a stronger $\mathcal{D}3$ dipole located at the symmetry axis. Reinforced by merging with several layers of secondary vorticity entrained by the primary vortices, the $\mathcal{D}3$ dipole finally detaches from the wall and moves in the opposite direction of the initial $\mathcal{D}0$ dipole. This lifting dipole is also observed in our simulations for the same Reynolds number (see Figure 3).

To conclude this section we emphasize some basic characteristics of the dipole interaction with infinite flat-walls:

1. the generation of secondary vorticity at the wall is the basic mechanism governing the flow evolution;
2. the flow is dominated by the primary vortices and the collision between secondary $\mathcal{D}1$ and $\mathcal{D}2$ dipoles is weak;
3. a lifting $\mathcal{D}3$ dipole can be obtained after several rebounds when the flow dissipation is low enough.

Different rebound phenomena will appear when finite aspect ratio flat walls are considered (see Section 5).

5. Dipole Impinging on Finite Aspect Ratio Flat Walls

5.1. Flow evolution

In this section, the ratio l/a will be varied for a fixed Reynolds number. We first present the results for $Re = 800$.

For the lowest considered parameter, $l/a = 0.5$, the vortex-obstacle interaction displays a totally different picture (Figure 4) than in the previous section.

Secondary vorticity is generated at the wall as previously ($t = 7$), but the vorticity layer can freely roll-up because of the limited extent of the obstacle. As a result, the secondary vortex ($t = 9$) is stronger and dipoles $\mathcal{D}1$ and $\mathcal{D}2$ move on larger radius trajectories ($t = 11$–19) to finally undergo a head-on collision at $t = 21$. This type of interaction was largely studied in the literature [3, 22, 24] and displays the classical characteristics: the dipoles $\mathcal{D}1$ and $\mathcal{D}1$ exchange partners ($t = 23-25$) and form two new dipoles ($\mathcal{D}3$ and $\mathcal{D}4$) which move along the direction perpendicular to the original one ($t \geq 25$). The lifting dipole ($\mathcal{D}3$) will leave the computational domain, while ($\mathcal{D}4$) will interact again with the obstacle. It is interesting to note that the symmetry of the flow is preserved and the dipole $\mathcal{D}4$ is moving exactly along the y-axis. The rebound of $\mathcal{D}4$ ($t > 29$) will generate new dipoles that are not strong enough to undergo head-on collisions—they evolve on circular paths near the obstacle.

The head-on collision and the generation of a strong lifting $\mathcal{D}3$ dipole is a very interesting feature of dipole interaction with walls. In order to explore the parameter range leading to the formation of a lifting dipole, simulations with $l/a = 1, 1.5, 2$ where conducted.

The results for $l/a = 1$ and 1.5 are shown on Figure 5. For $l/a = 2$ the flow evolution is very similar to that obtained for $l/a = 5$ (infinite flat wall) and therefore is not shown. The lifting dipole is obtained also for $l/a = 1$, with a lower intensity than for $l/a = 0.5$. A new interesting phenomenon is observed for $l/a = 1.5$: the lifting dipole (which is still symmetric) is completely trapped by the vorticity field of the dipole moving downwards ($t = 19-25$) and is almost steady. It will be finally dissipated by viscosity. We can conclude that $l/a = 1.5$ is the critical value for the existence of an upward-moving dipole for $Re = 800$.

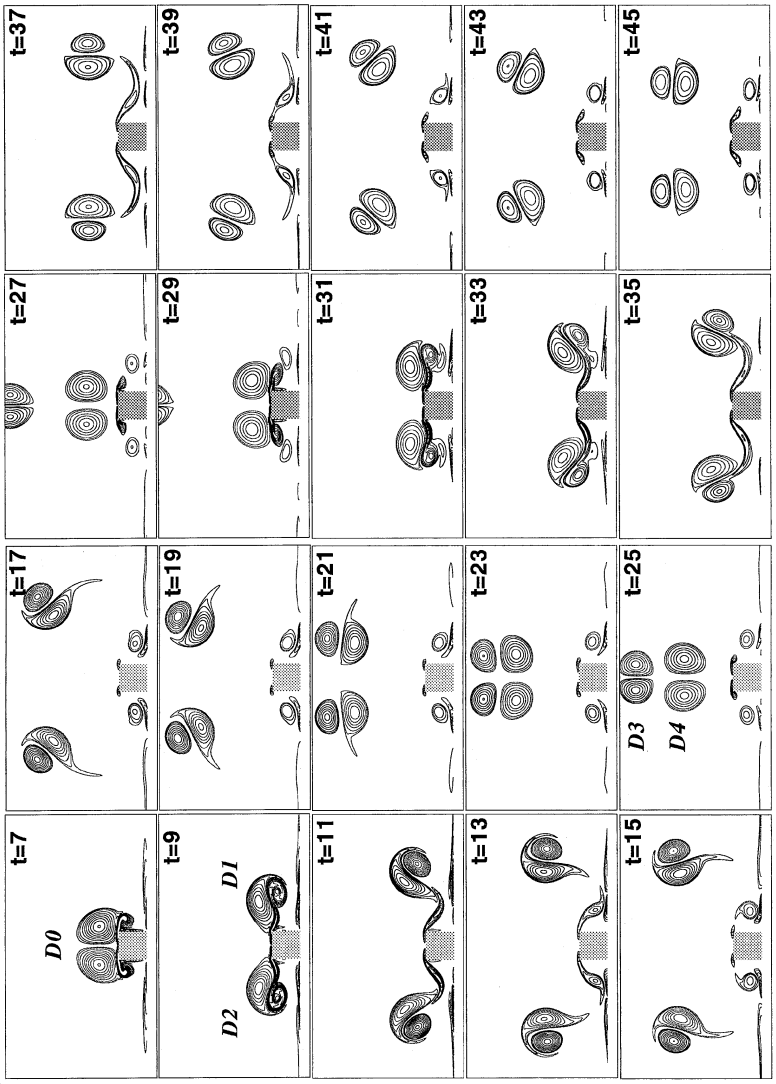

Figure 4. $Re = 800, l/a = 0.5$. Vorticity contours.

5.2. DIPOLES CHARACTERISTICS AND TRAJECTORIES

A synthetic picture of the flow evolution can be obtained by plotting the trajectories of vortices. The vortex centers (X, Y) for the primary (secondary) vortices are easily identified by the maximum (minimum) of vorticity in the right half-plane. Figure 6 compares trajectories for different l/a parameters and two Reynolds numbers ($Re =$ 800 and 1600).

When increasing l/a, the radius of the spiraling motion of vortex centers is decreasing and the secondary vortex is trapped near the obstacle. As a result, the

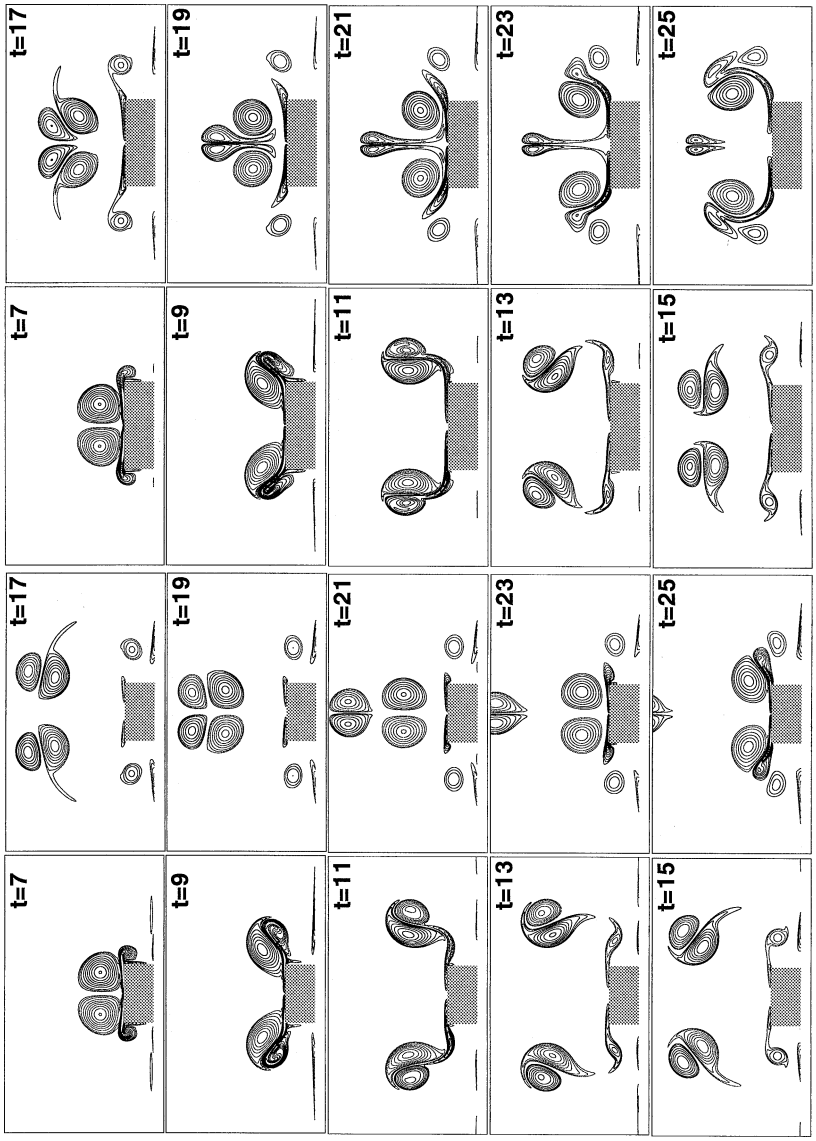

Figure 5. $Re = 800$, $l/a = 1.0$ (left) and $l/a = 1.5$ (right). Vorticity contours.

lifting dipole $\mathcal{D}3$ (resulting from the head-on collision of the dipoles $\mathcal{D}1$ and $\mathcal{D}2$—see Figure 4) is obtained only for l/a lower than a critical value (1.5 for $Re = 800$ and 2 for $Re = 1600$). We recall that the lifting dipole seen for $l/a = 5$ and $Re = 1600$ was the result of wall-generated vorticity and not of head-on dipole collisions (note the twisted trajectory of the secondary vortex for this case).

In order to quantify this observation, we calculate the relative circulation of the dipole $\mathcal{D}1$ (formed after the first rebound, see Figures 2–5) as the ratio $\Gamma_r = \Gamma_p / \Gamma_s$

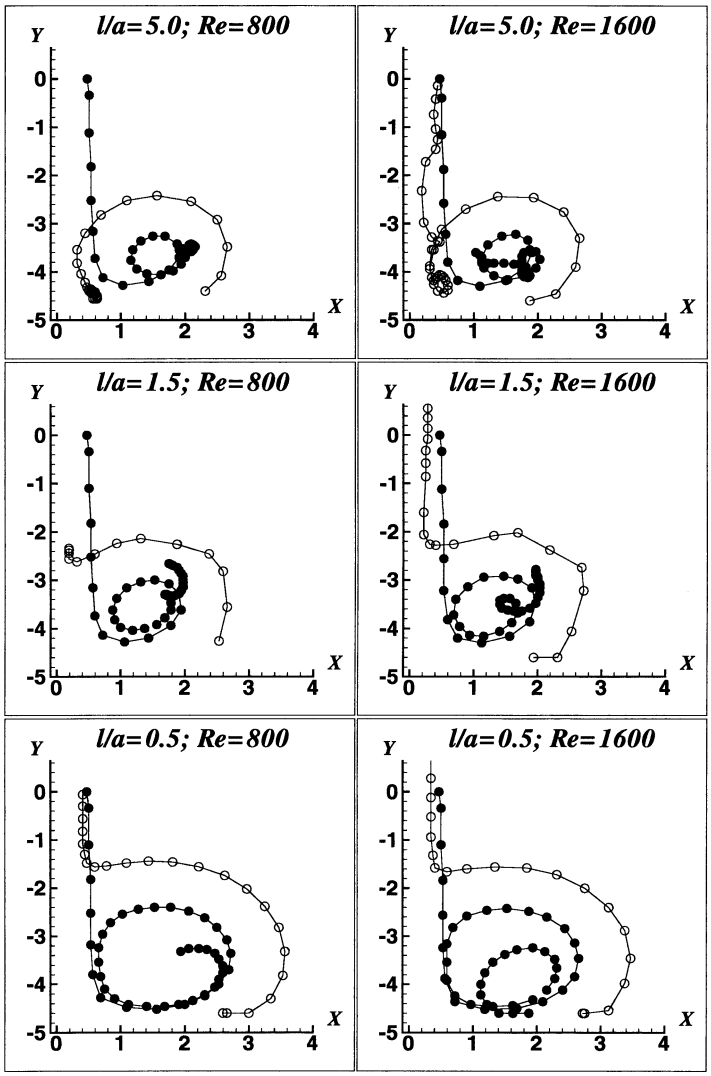

Figure 6. $Re = 800$. Trajectories of vortex centers in the right half-plane–filled symbols for the primary vortex and open symbols for the secondary vortex.

between the circulations of primary and secondary vortices of the dipole. The values (Table I) calculated just before the collision with $\mathcal{D}2$ suggest that partner exchange during the collision occurs only for $\Gamma_r < 1.8$. Orlandi [6] reported some numerical experiments with artificially created $\mathcal{D}1$ and $\mathcal{D}2$ dipoles; he concluded that partner exchange occurs for $\Gamma_r \approx 1$, a value that was not realistic for the dipole impinging on infinite flat wall. In this connection, it is interesting to note that the value $\Gamma_r = 2$ for $l/a = 2$ ($Re = 800$) is exactly the same found by Orlandi for the same case.

Another fundamental question we address is the relationship between the vorticity ω and the stream-function ψ characterizing the dipoles generated during the

Table I. Ratio $\Gamma_r = \Gamma_p / \Gamma_s$ between the circulations of primary and secondary vortices of the dipole $\mathcal{D}1$ obtained after the first rebound. Circulations are evaluated just before the collision with $\mathcal{D}2$.

	l/a				
	0.5	1.0	1.5	2.0	5.0
$Re = 800$	1.37	1.51	1.77	2.00	2.02
$Re = 1600$	1.27	1.38	1.55	1.80	1.82

flow evolution. For this purpose, dipoles $\mathcal{D}0$, $\mathcal{D}1$, $\mathcal{D}3$ and $\mathcal{D}4$ were isolated from the flow-field and the stream-function was computed by solving the Poisson equation $\Delta\psi = -\omega$ in the chosen rectangular window. The stream function was corrected afterwards [4] to get ψ in a frame of reference translating or rotating with the dipole. Corresponding 'scatter plots' are obtained by plotting ω as a function of ψ for grid-points lying inside the dipole. The results for $l/a = 0.5$ ($Re = 800$) are displayed on Figure 7.

$\mathcal{D}0$ is the initial dipole at time $t = 4$. The linear relationship (Equation 3) of the original Lamb–Chaplygin dipole is still verified. $\mathcal{D}1$ dipole displays a function $\omega(\psi)$ close to the well-known $sinh$ relationship (e.g. [9]) occurring in 2D vortical flows. It is interesting to note that the head-on collision between identical $\mathcal{D}1$ and $\mathcal{D}2$ dipoles leads to relatively different structures for $\mathcal{D}3$ (upwards moving dipole) and $\mathcal{D}4$ (downwards moving dipole). The former displays an almost linear $\omega(\psi)$ scatter, while the same relationship is closer to a non-linear $\sin h$ distribution for the latter.

6. Final Discussion and Conclusion

When experimentally studying the interaction between vortex dipoles and flat walls, van Heijst and Flór [23] had the intuition of a head-on collision and partner exchange between secondary dipoles generated after the first rebound. Numerical simulations of Orlandi [6] invalidated this scenario, showing that, for 'infinite' flat walls, the secondary vortices are not strong enough to allow such interactions (the relative circulation $\Gamma_r = \Gamma_{primary} / \Gamma_{secondary}$ was too large).

Our present simulations show that the scenario of van Heijst and Flór [22, 23] takes place when finite aspect ratio rectangular obstacles are considered. Due to the limited extent of the obstacle, stronger secondary vortices are allowed to develop by the roll-up of the vorticity layer. For ratios l/a (between the obstacle half-width and vortex dipole radius) lower than a critical value (depending on the Reynolds number), secondary dipoles undergo head-on collisions and partner exchange. This corresponds to ratios $\Gamma_r < 1.8$. A lifting dipole is obtained, moving in the opposite direction of the original dipole. For the considered

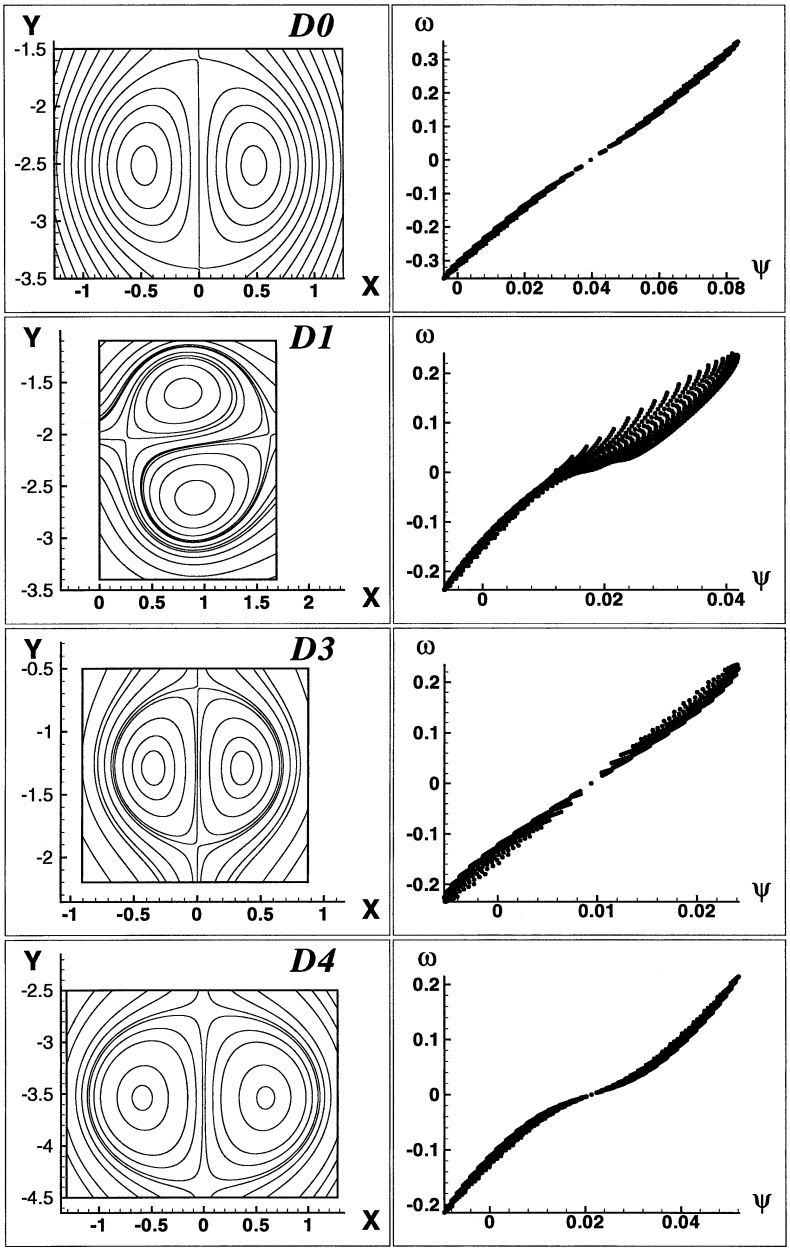

Figure 7. $Re = 800$, $l/a = 0.5$. Contours of the corrected stream-function (left) and corresponding scatter plots (right) for the dipoles appearing on Figure 4.

Reynolds numbers, only one partner exchange is observed, corresponding to the first rebound.

Since the generation of the lifting dipole can have interesting practical consequences, we conclude by suggesting some 'strategies' for the passive control of

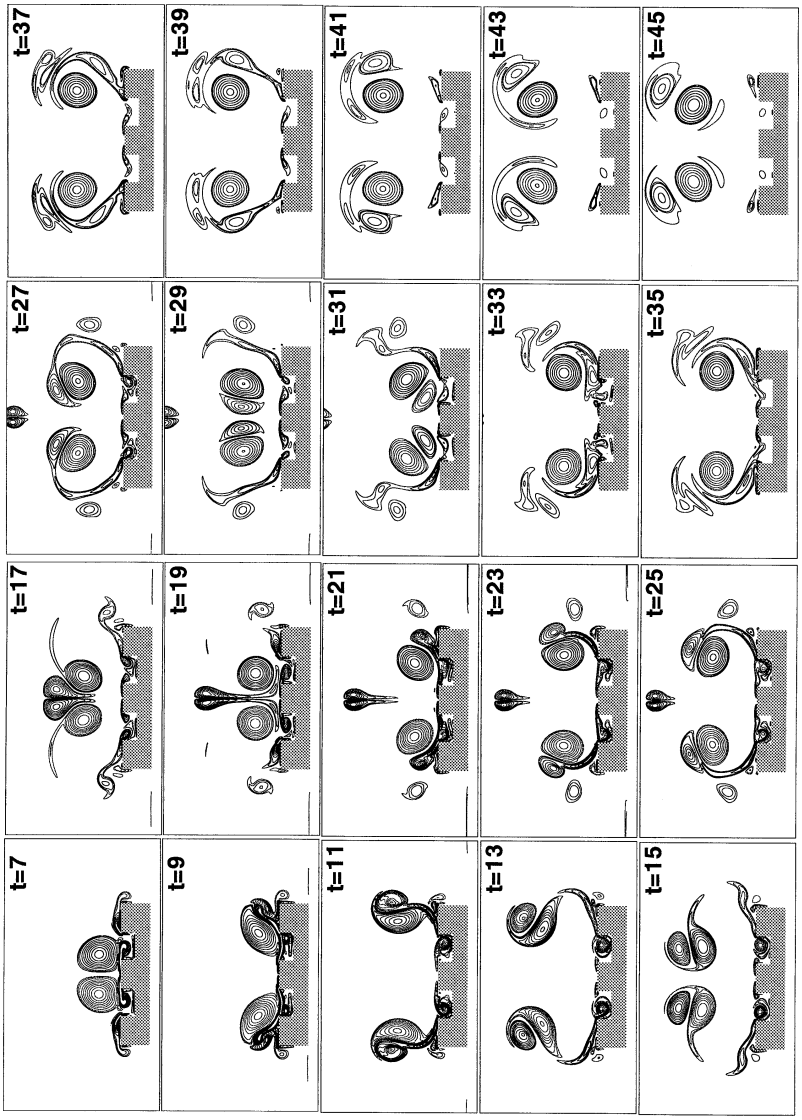

Figure 8. $Re = 1600$, $l/a = 3.0$. Dipole interaction with an obstacle with crenellations. The lifting dipole movement is inhibited.

such vortex-wall interaction. Active control of such flows are usually used to test control methodologies developed for wall bounded flows (e.g. [25]). Figure 8 shows the dipole interaction with more complicated shapes. The formation of the lifting dipole can be inhibited by using an obstacle with crenellations; for $Re = 1600$, the lifting dipole is almost steady and rapidly dissipated for $l/a = 3$, compared to $l/a = 2$ for the rectangular obstacle. We must emphasize at this point that the used numerical method easily allows to model more complicated obstacle shapes.

Acknowledgments

This study is a part of a work supported by IFP (Institut Français du Pétrole) which is gratefully acknowledged for financial support. The NTMIX code is developed in the framework of CRCT (Centre de Recherche en Combustion Turbulente).

References

1. Lamb, H., Hydrodinamics. Cambridge University Press, London (1932).
2. Meleshko, V.V. and van Heijst, G.J.F., On Chaplygin's investigation of two-dimensional vortex structures in an inviscid flow. *J. Fluid Mech.* **272** (1994) 157–182.
3. Couder, Y. and Basdevant, C., Experimental and numerical study of vortex couples in two-dimensional flows. *J. Fluid Mech.* **173** (1986) 225–251.
4. Nguyen Duc and J.-M., Sommeria, J., Experimental characterization of steady two-dimensinal vortex couples. *J. Fluid Mech.* **192** (1988) 175–192.
5. Flór, J. B. and van Heijst, G.J.F., An experimental study of dipolar vortex structures in a stratified flow. *J. Fluid Mech.* **279** (1994) 101–133.
6. Orlandi, P., Vortex dipole rebound from a wall. *Phys. Fluids* **A2** (1990) 1429–1436.
7. Orlandi, P., Vortex dipoles impinging on circular cylinders. *Phys. Fluids* **A5** (1993) 2196–2206.
8. Verzicco, R., Flór, J.B., van Heijst, G.J.F. and Orlandi, P., Numerical and experimental study of the interaction between a vortex dipole and a circular cylinder. *Exp. Fluids* **18** (1995) 153–163.
9. van Geffen, J.H.G.M. and van Heijst, G.J.F., Viscous evolution of 2D dipolar vortices. *Fluid Dyn. Res.* **22** (1998) 191–213.
10. Carnevale, G.F., Velasco Fuentes, O.U. and Orlandi, P. Inviscid dipole-vortex rebound from a wall or coast. *J. Fluid Mech.* **351** (1997) 75–103.
11. Stossel, A., An efficient tool for the study of 3D turbulent combustion phenomena on MPP computers. In: *Proceedings of the hight performance computing and neworking 95 Conference*. Springer-Verlag, Berlin (1995) pp. 306–311.
12. Williamson, J. H., Low storage Runge-Kutta schemes. *J. Comput. Phys.* **35** (1980) 48–56.
13. Lele, S.K., Compact finite difference schemes with spectral-like resolution. *J. Comput. Phys.* **103** (1992) 16–42.
14. Poinsot, T. and Lele, S. K., Boundary conditions for direct simulations of compressible viscous flows. *J. Comput. Phys.* **101** (1992) 104–129.
15. Peskin C.S., Flow patterns around heart valves: A numerical method. *J. Comput. Phys.* **10** (1972) 252–271.
16. Goldstein, D., Handler R. and Sirovich, L., Modeling a no-slip flow boundary with an external force field. *J. Comput. Phys.* **105** (1993) 354–366.
17. Saiki, E.M. and Biringen, S., Numerical simulation of a cylinder in uniform flow: Application of a virtual boundary method. *J. Comput. Phys.* **123** (1996) 450–465.
18. Angot, P., Bruneau, C.-H. and Fabrie P., A penalization method to take into account obstacles in incompressible viscous flows. *Numerische Mathematik* **81**(4) (1999) 497.
19. Mohd-Yusof, J., Combined immerse-boundary/B-spline methods for simulations of flows in complex geometries. *CTR Annual Research Briefs* (1997) pp. 317–327.
20. Verzicco, R., Mohd-Yusof, J., Orlandi, P. and Haworth, D., Large eddy simulation in complex geometric configurations using boundary body forces. *AIAA J.* **38**(3) (2000) 427–433.
21. Fadlun, E. A., Verzicco, R. and Orlandi, P., Combined immersed-boundary finite-difference methods for three-dimensional complex flow simulations. *J. Comput. Phys.* **161** (2000) 35–60.
22. van Heijst, G.J.F. and Flór, J.B., Dipole formation and collisions in a stratified fluid. *Nature* **340** (1989) 212–215.

23. van Heijst, G.J.F. and Flór, J.B., In: Nihoul, J.C.J. and Jamart, B.M. (eds.), *Mesoscale/Synoptic Coherent Structures in Geophysical Turbulence*. Elsevier, Amsterdam, (1989) pp. 591–608.
24. Velasco Fuentes, O. U. and van Heijst, G. J. F., Collision of dipolar vortices on the beta plane. *Phys. Fluids* **7** (1995) 2735–2750.
25. Koumoutsakos, P., Active control of vortex-wall interactions. *Phys. Fluids* **9** (1997) 3808–3816.